



Fabrication of graded alumina by spark plasma sintering

Eszter Bódis¹ · Zoltán Károly¹

Received: 23 April 2021 / Accepted: 7 August 2021 / Published online: 18 August 2021
© The Author(s) 2021

Abstract

Functionally graded materials (FGMs) attract considerable interest in materials science and industry, since their composition or morphology gradually changes along their length, width, or height, which provides new approach for the development of multifunctional materials. In this paper, we studied the fabrication of a gradient microstructure in alumina (Al_2O_3) by spark plasma sintering (SPS). During the SPS process, the applied asymmetric graphite tool configuration causes a large temperature gradient, which results in a gradually changing morphology in Al_2O_3 ceramics. The local temperatures were quantitatively measured through extra thermocouples during SPS processes with various asymmetric configurations. In the most asymmetric configuration, a maximum vertical temperature difference of 225 °C was detected within the sample treated at a sintering temperature of 1300 °C and a pressure of 25 MPa applied 200 °C·min⁻¹ heating rate. The microstructure investigations demonstrated the morphology gradient in the ceramic: one part of the Al_2O_3 exhibited fine, nanostructured morphology with large open and permeable pores, whereas the other part was solid without pores. Our investigations show that a gradient Al_2O_3 ceramic can be produced with a single-step SPS process, which offers new directions in FGMs research. With an asymmetric sintering configuration and the sintering conditions, the structure of the ceramic, such as porosity, can be designed according to the requirements of the application area.

Keywords Alumina · Graded porosity · Thermal gradient · SPS · Functionally graded material (FGM)

1 Introduction

Functionally graded materials (FGMs) have attracted considerable attention in materials research and the industry because of their gradually changing structure and properties, which makes them exceptionally suited for various applications [1, 2]. FGMs can be designed by structure, composition, or morphology with respect to the special requirements of the particular application area ranging from nuclear energy, engineering, optics, aerospace, electronics, and energy conversion applications to biomaterials [3]. The properties of the material vary gradually or in segments throughout the cross section of the sample.

FGMs can be prepared by various processes, such as deposition methods, infiltration, and tape and slip casting depending on the application area [1, 4], but these processes consist of several

steps. However, spark plasma sintering (SPS), a well-known powder metallurgy processing method, offers a promising approach to making FGMs in a single step [5, 6], due to its unique heating method [7–10]; the modification of the spatial distribution of the effective current per unit area results in a temperature gradient within the sample [11]. This creates the possibility of (a) joining different types of materials into a single part [7]; (b) producing a monolithic sample with a dissimilar phase composition [12]; and more importantly with regard to the present paper (c) fabricating sintered bodies with controlled porosity. In the latter case, the various parts of the sample exposed to different sintering temperatures acquire different degrees of porosity; i.e., a porosity-graded part can be formed [13].

Inhomogeneous current distribution and thus a thermal gradient can be produced by several methods during the SPS process depending on material properties, the applied sintering conditions, and the shape, size, and position of the graphite tools, as well. The possible alternatives for controlling the temperature gradient in SPS technique for fabrication FGMs are reviewed by S. Grasso [14]. Anselmi-Tamburini et al [15] observed inhomogeneous current distribution in alumina and copper samples, due to their different electrical

✉ Eszter Bódis
bodis.eszter@ttk.hu

¹ Institute of Materials and Environmental Chemistry, Research Centre for Natural Sciences, Magyar Tudósok Körútja 2, Budapest H-1117, Hungary

conductivity. Dudina et al [4] showed that the applied high heating rate or uniaxial pressure resulted in inhomogeneous temperature distribution inside the samples. Morin et al [16] generated a temperature gradient with the use of an unconventional graphite tool (the thickness of the graphite mold varied in the axial direction). They assumed that the temperature gradient varied strongly depending on geometry of the graphite die. Several studies also suggested an existing temperature gradient in the sample even with conventional SPS graphite tools during heat treatment in the case of an asymmetric vertical arrangement [12, 16, 17]. Belmonte et al [12] produced microstructure-graded Si_3N_4 samples with dissimilar phase composition as a result of an asymmetric graphite piston configuration. Hulbert et al. [18] combined various materials by in situ reactions to develop tailored structured B_4C -Al, TiB_2 - B_4C , and HfB_2 -SiC ceramic composites. In our previous study [19], we also assumed a temperature gradient during the SPS process, since the SiC-ZrO₂ composites crystallized in different phase compositions at the opposite sides of the sintered bodies. Although numerous studies have reported on the development of a temperature gradient in the sample during the SPS process, we still have rather limited knowledge on the extent of the temperature difference inside the sample during sintering. A deeper investigation on it with exact temperature measurements was performed by Morin et al [16]; however, they used asymmetric graphite mold instead of asymmetric sample position. In this paper, we studied the temperature gradient in a sintered Al_2O_3 sample as model material varying the position of the sample in the graphite tool and determine the relationship between the temperature gradient and the major operating parameters including sintering temperature, heating rate, sintering time, and uniaxial pressure.

Selecting Al_2O_3 as model material was reasoned by being produced in the largest quantity among advanced ceramics. Moreover, its application field can be greatly broadened as functionally graded material especially in medicine [20–23]. The good mechanical properties combined with bioinertness make alumina an appealing material of choice for several medical applications such as bearings in hip replacement [24] or dental implants [25], but a graded microstructure would be an additional advantage.

In our work, we not just reveal the temperature gradients inside the sample in different positions but also demonstrate how to take advantage of this phenomenon to prepare FGM alumina.

2 Experimental

2.1 Synthesis of Al_2O_3 nanoparticles

Nanosized crystalline Al_2O_3 powder was prepared by the hydrothermal method based on the study of [26]. First 0.7 M

aluminum nitrate nonahydrate [$\text{Al}(\text{NO}_3)_3 \cdot 9\text{H}_2\text{O}$] was dissolved in 200 ml of distilled water. Then 0.3 M ammonium hydroxide solution was added dropwise to the solution until it reached pH 9. As a result, gelatinous white aluminum hydroxide (boehmite) precipitated. The precipitate was filtered and washed three times with distilled water and finally dried in an oven at 90 °C in air for 24 h. This powder was ground in a high-purity alumina ball mill in alcohol for 1 h and dried again at 50 °C for 12 h. The dried aluminum hydroxide powder was calcined at 700 °C for 1 h. The X-ray diffraction (XRD) and scanning electron microscopy (SEM) analysis confirmed that γ - Al_2O_3 was obtained with an average particle size of ~200 nm.

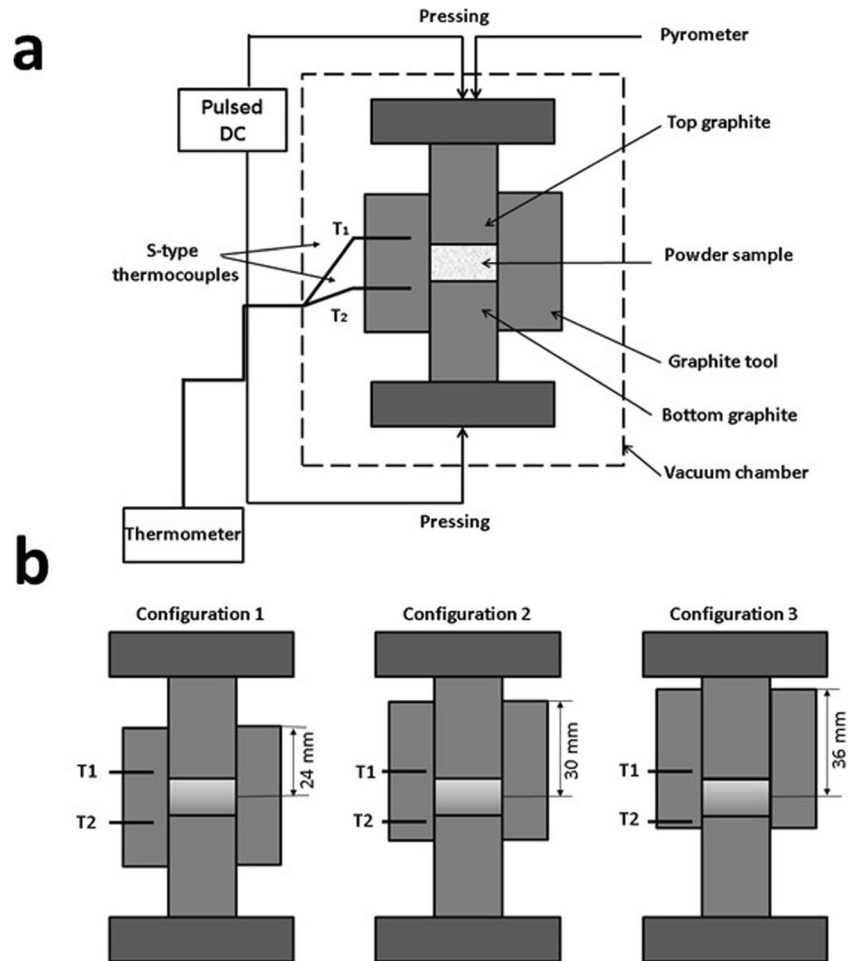
2.2 Synthesis and analysis

The Al_2O_3 powder was consolidated with the use of SPS equipment (HPD25, FCT System GmbH, Germany). We studied three graphite tool configurations, illustrated in Fig. 1. *Configuration 1* (standard configuration) shows a symmetric position of the graphite pistons, and the powder was placed in the center position (24 mm from the top and bottom), similarly to standard sintering. In *configuration 2* and 3, the powder samples were shifted vertically downward into an asymmetric position (Fig. 1b). In *configuration 2*, the sample was placed at the bottom part of the graphite mold, with the center of the powder 30 mm from the top, while in *configuration 3*, the center of the sample was still lower at 36 mm from the top (Fig. 1b). In order to determine the temperature gradients in the samples, two S-type thermocouples were placed at the top (T_1) and bottom (T_2) parts of the samples, respectively. The thermometer probes were inserted into the wall of the graphite tools, 2 mm from the powder sample, as it is shown by the Fig. 1. The sintering temperature, as usual, was also measured by the pyrometer, which measures directly the temperature of the upper graphite piston through a hole.

The sintering settings, including temperature and pressure, were varied in the experiments. The settings are summarized in Table 1. The nanosized Al_2O_3 powder was sintered for 3 min at 1200 °C and 1300 °C. Heating rate was also investigated in configuration 3 for the given condition at 1300 °C and 25 MPa. The values were set for 100, 150, and 200 °C·min⁻¹. The temperatures were basically controlled by the pyrometer. During heat treatment, the samples were in a 10⁻² mbar vacuum, pressed with 25 and 50 MPa uniaxial pressure at each temperature. All tests were carried out with a pulse sequence of 12: 6 ms (on:off). The diameter of the sintered specimens was 20 mm. Discussion of the results was based on a single sintering test for each setting.

Displacement and the rate of shrinkage were also monitored. The relative density of the sintered samples was determined by Archimedes' method. The crystalline phase composition of the sample was determined with a Philips PW1830

Fig. 1 a) Schematic representation of the arrangement SPS sintering equipment b) standard and asymmetric graphite configurations



X-ray diffractometer with Cu K α radiation at 40 kV and 35 mA. The microstructure was investigated on the cross section of the fractured surfaces of the samples by scanning electron microscopy (SEM, Zeiss EVO XY) at various magnifications.

3 Results and discussion

3.1 The temperature gradient during the SPS process

Figure 2 shows the temperatures at the top (T_1) and the bottom (T_2) of the samples recorded by the thermocouples as a function of the pyrometer temperature values for the various

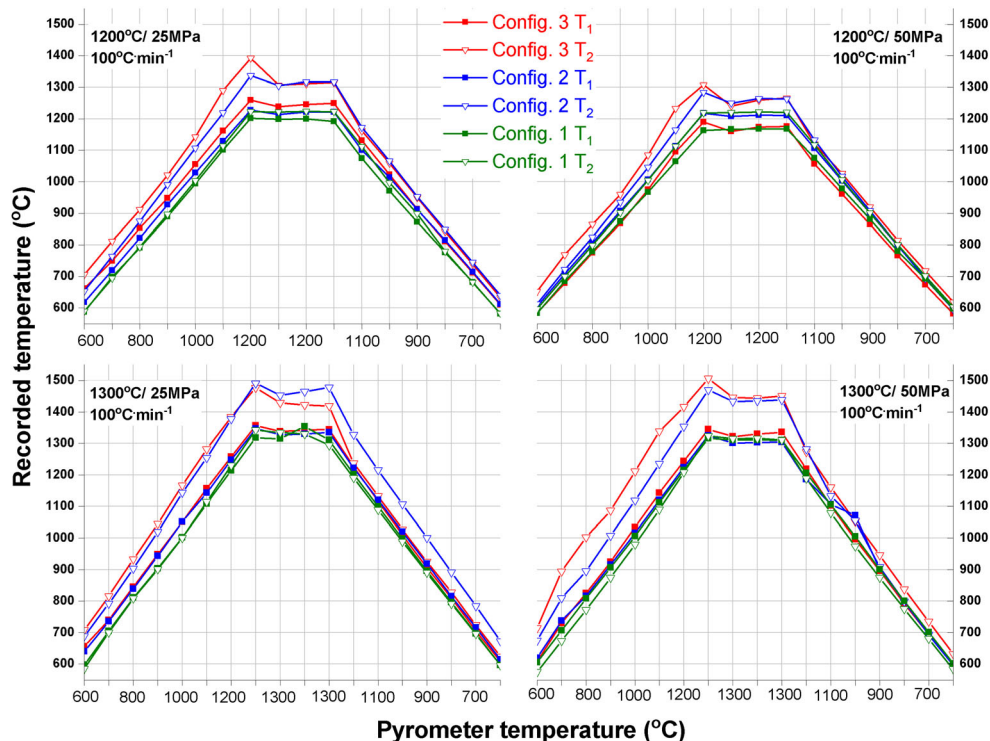
configurations and operating conditions. The green, blue, and red curves represent configuration 1, 2, and 3, respectively.

In configuration 1 (“standard”), the detected temperatures (T_1 and T_2) were almost identical and equal to the temperature measured by the pyrometer. By contrast, the asymmetric position of the samples resulted in a significant temperature difference between the opposite parts of the sample during sintering. In addition, the increased asymmetric position led to a higher temperature difference. The bottom temperature (T_2) was always higher than the temperature of the upper part (T_1), presumably due to the increased local current density at the bottom of the die [11]. The maximum vertical temperature gradient was detected for configuration 3 in each setting. For

Table 1 The applied sintering settings

Sintering settings											
Temperature (°C)	1200					1300					
Graphite tool configuration	1	2	3	1	2	3	1	2	3	1	2
Uniaxial pressure (MPa)	50	25	50	25	50	25	50	25	50	25	50

Fig. 2 Top (T_1 full squares) and bottom (T_2 empty triangles) temperatures of the samples as a function of the pyrometer temperature values. The green, blue, and red curves represent configuration 1, 2, and 3, respectively



the sample sintered at 1300 °C with a pressure of 50 MPa, the temperature (T_2) reached 1506 °C at the bottom part, resulting in a thermal difference of 172 °C in the sample. For the samples treated with the same sintering conditions, the obtained thermal gradients were 145 °C and 10 °C in configuration 2 and 1, respectively. A smaller but definite difference in the temperature of the opposite parts exists from the beginning of heating, and it gradually increases with increasing temperature. In addition, similarly to Morin et al.'s findings [16], we recorded larger temperature differences during the heating and holding periods than during cooling, especially at 1300 °C and 50 MPa (Fig. 2). Whereas in the heating and also in the holding segments, differences of approximately 50 °C and 150 °C were detected for configuration 2 and 3, respectively, in the cooling segments, they were only around 20 °C and 50 °C. The reduced temperature gradient can be attributed to the densification process, since as the particles get closer to each other, Joule-heating and current density get lower, as well.

The heating rate also affected the temperature difference. Increasing the heating rate from 100 to 200 °C, the temperature difference also almost doubled in the sample (Fig. 3). In addition, the difference did not decreased during the 3 min holding period as was suggested by Hulbert [18].

Not only the temperature differences of the two parts of the samples were higher at different configurations, but both parts of the sample reached a higher temperature in a more asymmetric position as compared to the “standard” one. We carried out sintering tests applying two different pressures, but it

seemingly did not have an effect on the temperature of the samples.

Figure 4 a–d show the shrinkage rate of the samples with respect to the temperature recorded by the pyrometer under various sintering conditions for the different configurations.

Comparing configuration 1 and 2, we can find differences mainly in the intensity of the peaks, but the courses of the shrinkage are similar (Fig. 4). Most intensive shrinkage occurs at ~1000 °C. It can probably be attributed to the $\gamma \rightarrow \alpha$ - Al_2O_3 phase transformation, which results in a volume reduction of

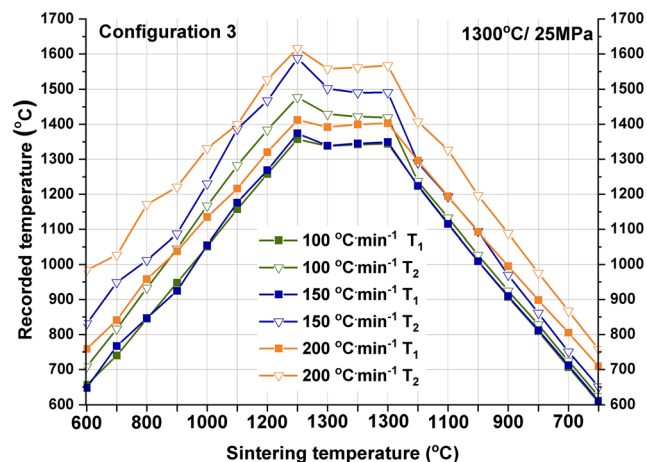


Fig. 3 Top (T_1 full squares) and bottom (T_2 empty triangles) temperatures of the samples as a function of the pyrometer temperature values with different heating rates. The orange, blue, and green curves represent the 200, 150, and 100 °C·min⁻¹ heating rates, respectively

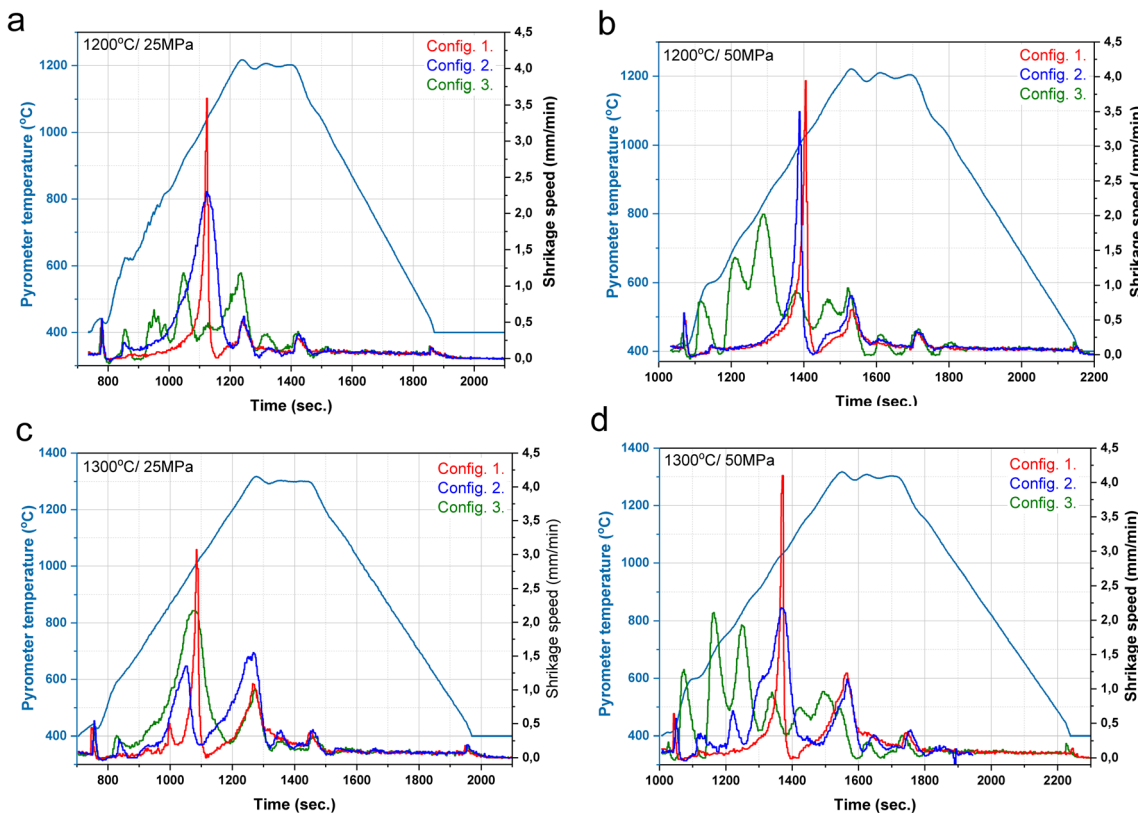


Fig. 4 Shrinkage speed of the sintered bodies at various sintering conditions (a) 1200 °C/ 25 MPa; (b) 1200 °C/ 50 MPa; (c) 1300 °C/ 25 MPa; (d) 1300 °C/ 50 MPa) with 100 °C·min⁻¹ heating rate

~10 % [27]. In contrast, for the samples sintered in configuration 3, we cannot observe such intensive shrinkage peak at ~1000 °C, but peaks with smaller intensity occur below that temperature. Furthermore, they are more obvious for samples exposed to a pressure of 50 MPa (Fig. 4b, d). However, we must keep in mind that at higher heating rate, the mean temperature of the sample is higher than as it is indicated by the pyrometer. While there is less shrinkage in the asymmetric configurations, it occurs in a wider temperature range. We think this effect can be attributed to the temperature gradient within the sample, since phase transformation and densification take place gradually in time within the sample. Also, it starts earlier in the bottom part, which has a higher temperature resulting in dissimilar shrinkages in the samples.

3.2 Effect of temperature gradient on the microstructure of the sintered Al₂O₃ samples

The relative densities of the samples sintered in different sintering conditions were determined by Archimedes method in distilled water, and the obtained values are shown in Fig. 5. The values vary in quite a wide range, between 48 and 87 %. Due to the supposedly graded micro- and pore structure, these values refer to an average.

The bar chart clearly shows increasing density as a function of sintering temperature and the applied pressure. It also

shows that a 100 °C temperature increase leads to more intensive sintering than a twofold increase in pressure on the graphite pistons. More importantly, under a certain temperature and pressure, density increased. The samples farther from the standard symmetric position exhibited higher relative density. The highest relative density (87 ± 0.8 %) was reached for the sample sintered at 1300 °C with 50 MPa in configuration 3, where the highest local temperature was detected. The sample

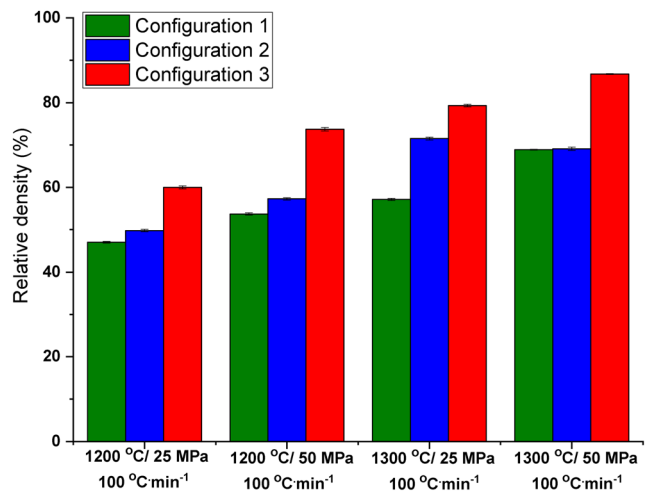


Fig. 5 Relative density of the samples produced with various sintering conditions

sintered under the same conditions in configuration 1 had a relative density of $69 \pm 0.7\%$. The trend can be attributed to the higher temperature difference between the bottom and the upper part of the sample.

Phase composition and transformation during the sintering procedures were analyzed by XRD. We compared the phase composition of the initial powder and the heat-treated samples and found that $\gamma \rightarrow \alpha\text{-Al}_2\text{O}_3$ phase transformation occurred during sintering (Fig. 6a) in all the samples. Furthermore, it was also supported by the intense peak of the shrinkage speed parameter at $1000\text{ }^\circ\text{C}$.

Since sintering temperature also affects the crystalline size of the bulk material and the temperature was different on opposite sides of the samples, the crystalline sizes of both sides of the samples were calculated by the Scherrer equation. The crystalline size on the top side of the samples was consistently smaller than on the bottom side for all the samples. Furthermore, crystalline size increased with the asymmetry of the graphite tool configurations, as well. Fig. 6 b and c illustrate the diffraction patterns for the given series of samples sintered at $1300\text{ }^\circ\text{C}$ under a pressure of 50 MPa in different configurations, where the increasing intensity and the narrowing diffraction peaks refer to larger crystallite size.

For these samples, the average crystalline sizes on the top and at the bottom were 141 and 165 nm , 219 and 543 nm , and 275 and 985 nm in configuration 1, 2, and 3, respectively. The difference in crystallite sizes is illustrated in a higher magnification in Figure 6c, which shows the characteristic diffraction peak of Al_2O_3 corresponding to the $[104]$ reflection. Both the upper and bottom values follow an increasing trend that is in line with the achieved higher temperature with increasing heating rate and temperature as a consequence.

We investigated the microstructure of the samples by SEM to determine the effects of (i) the various graphite tool configurations and (ii) the applied sintering conditions on the structure of the samples. We examined the whole cross section of the fractured surfaces of the samples from top to bottom. Figure 7 shows the microstructure of all the samples sintered under the same conditions ($1300\text{ }^\circ\text{C}$, 25 MPa , and $100\text{ }^\circ\text{C}\cdot\text{min}^{-1}$).

The sample in symmetric position (configuration 1) shows a uniform microstructure through the whole cross section. The bulk consists of almost nanometric particles with a size similar to the particle size of the initial Al_2O_3 powder (200 nm), and its increased porosity suggests a small degree of densification. The latter can be attributed to the relatively low sintering

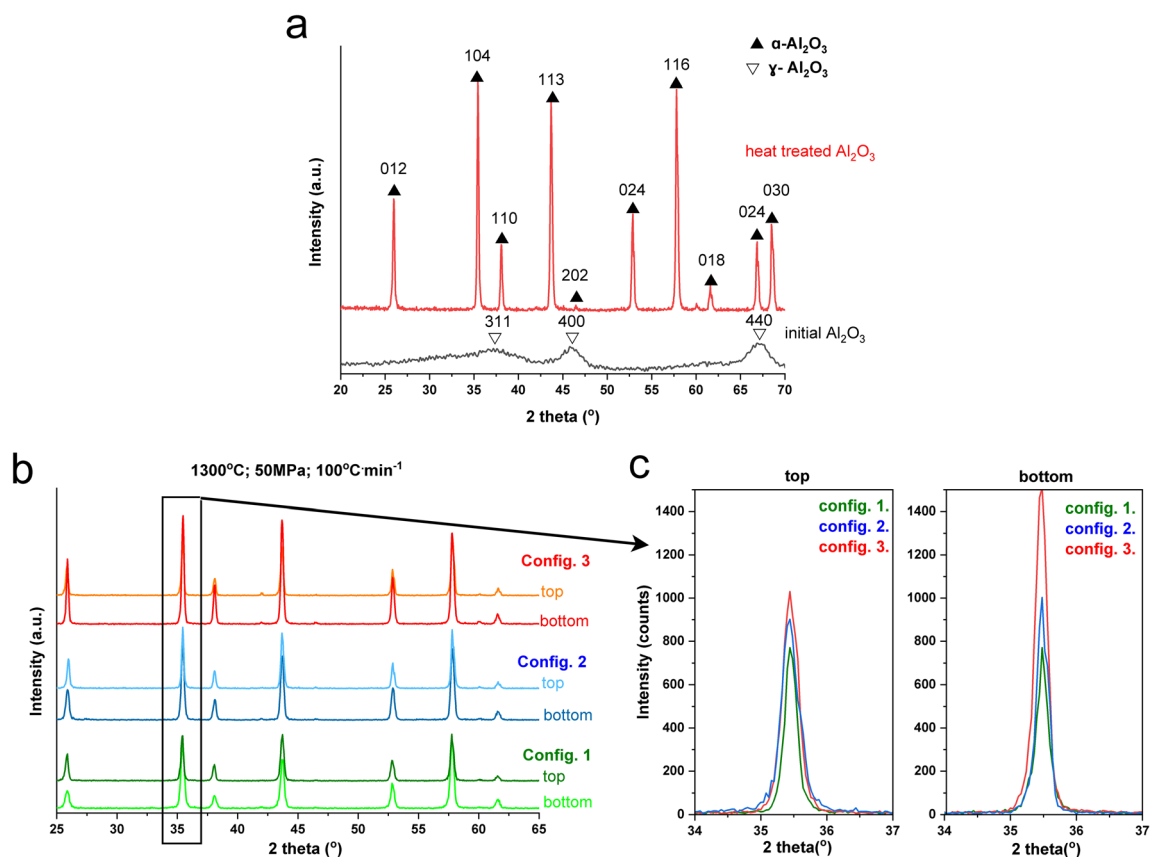


Fig. 6 a Phase composition of the initial and heat-treated sample. b Phase composition of $1300\text{ }^\circ\text{C}/50\text{ MPa}$ samples heat-treated in various configurations. c The characteristic diffraction peak of Al_2O_3 corresponding to

the $[104]$ reflection illustrates the crystalline size variation according to the different configurations

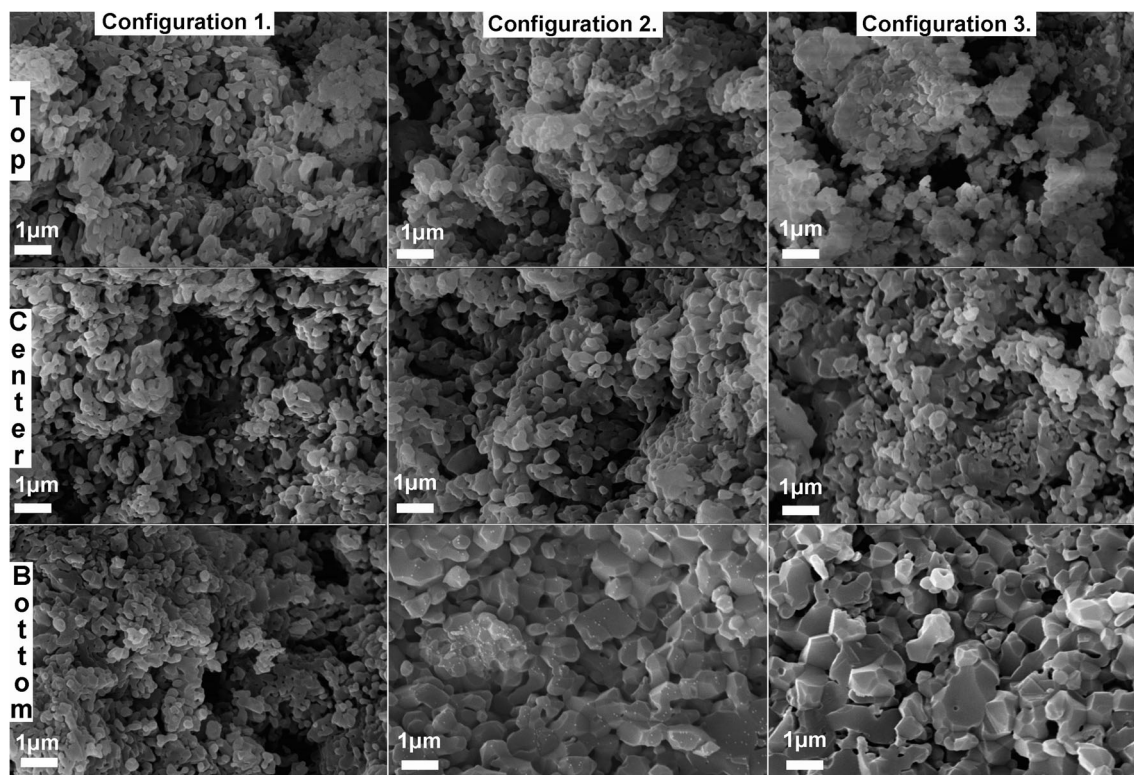


Fig. 7 Fractured surfaces of the samples treated with various graphite tool configurations at 1300 °C and 25 MPa

temperature applied (1300 °C), which was not exceeded considerably either on the top (1311 °C) or the bottom (1315 °C) part of the sample.

However, for samples in asymmetric positions (configuration 2 and 3), remarkable changes can be detected between the top and bottom parts in terms of grain size and porosity distribution. The grain sizes in the upper region of the samples are approximately identical to that of the standard configuration, as can be expected, considering that there was not a large difference in the detected top temperature (T_1). In contrast, the bottom region of the samples consists of much larger grains. In configuration 2, neck formation can be observed between the ~ 700 nm large particles, while grain size increased further up to around 1–2 μm in configuration 3. For both configurations, the degree of densification gradually increased towards the bottom part, resulting in reduced porosity at the bottom region. Based on the relative density values, total porosity was 29 % in this sample with configuration 2 (Fig. 5). According to the SEM analysis, pore distribution was inhomogeneous in the cross section, and the pore structure is open and permeable in the whole sample. For the sample treated in configuration 3, average porosity decreased to 21%, but while the pores are interconnected throughout the sample, pore size decreased towards the bottom part.

Figure 8 demonstrates the effect of the different sintering conditions (applied temperatures and pressures) on the

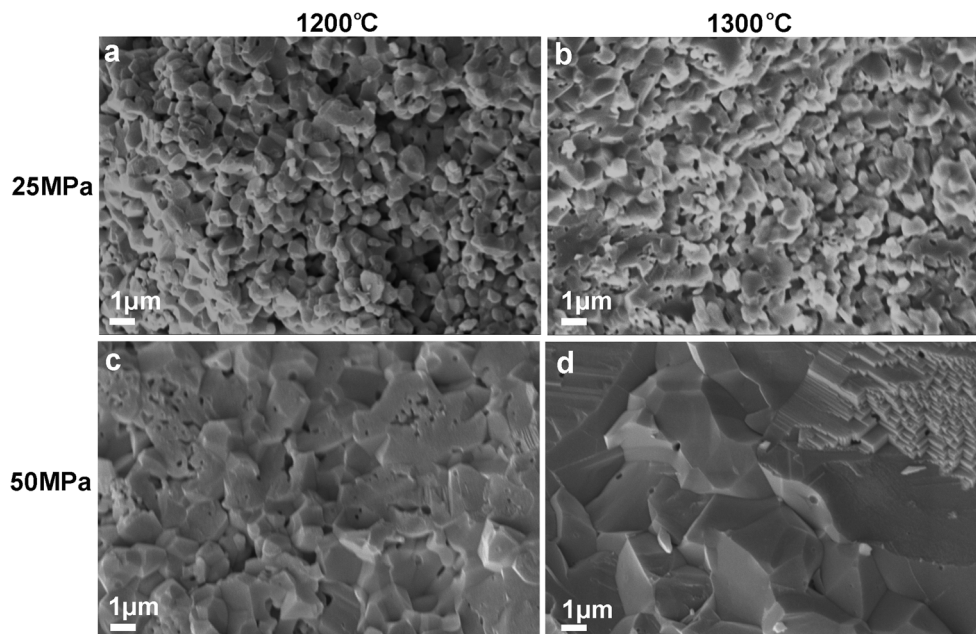
microstructure. The images were taken of the bottom part of the samples sintered in configuration 3, where the highest local temperature occurred during sintering.

Regardless of the temperature, the densification was poor at the bottom part with the lower pressure of 25 MPa and the sintering process remained in the neck formation section, which led to an open pore structure (Fig. 8a, b). Increasing the sintering pressure from 25 to 50 MPa led to an increase in the density of both samples (Fig. 8c, d). Moreover, the structure of the sample sintered at the maximum temperature and pressure was nearly pore-free (Fig. 8d). Our microstructure investigations showed that graded Al_2O_3 ceramics with various microstructures can be developed with asymmetric graphite tool configurations and different sintering conditions. This technology may provide new aspects in several application areas like piezoelectric science as piezoelectric properties of porous ceramics can be enhanced [28]. However, to increase the aforementioned feature of ceramics and other materials, special surface modification may be also required [29].

4 Summary

In this paper, we demonstrated a new approach to synthesizing functionally graded ceramics by spark plasma sintering, using alumina powder as model material.

Fig. 8 SEM images of the bottom part of the samples in asymmetric position by various sintering conditions applying $100\text{ }^{\circ}\text{C}\cdot\text{min}^{-1}$



During heating, an in situ thermal gradient was generated inside the sample when the graphite tools were placed in an asymmetric position, which resulted in a continuously changing microstructure in the cross section of the Al_2O_3 sample. The obtained temperature gradient and microstructure were studied systematically when the asymmetric position of the graphite tools and sintering conditions, including temperature, pressure, and heating rate, were varied.

The experimental results showed that as asymmetry increased in the graphite tool configuration, a relatively large vertical temperature gradient developed within the sample. While the top temperature of the samples was nearly identical to the set temperature in each test, the temperature at the bottom significantly differed. Both greater asymmetry and higher sintering temperature increased the temperature difference between the opposite part of the sample. The largest temperature differences ($225\text{ }^{\circ}\text{C}$) was recorded for configuration 3 (the most asymmetric position of the graphite tools), with a temperature of $1300\text{ }^{\circ}\text{C}$ and a pressure of 25 MPa applied $200\text{ }^{\circ}\text{C}\cdot\text{min}^{-1}$ heating rate.

The developed large temperature gradients caused discontinuous densification and consequently graded microstructures in the vertical cross section. Crystalline size and pore structure also exhibited a gradual change through the vertical cross section as a result of the temperature gradient. The microstructure of the obtained sample consists of a nanosized grains with open and interconnected pore structure on one part and a pore-free, completely solid structure on the opposite part of the sample. Although this study was performed on alumina, this method also works for other type of ceramics or ceramic matrix composites to attain FGM structure.

Acknowledgements The authors thank Gábor Babos for the technical assistance in the implementation of the extra temperature monitoring system for the SPS equipment.

Code availability Not applicable

Author contribution Eszter Bódis: Conception making, investigation, writing
Zoltán Károly: Results evaluation, writing

Funding Open access funding provided by ELKH Research Centre for Natural Sciences. The project was supported by the Hungarian National Research, Development and Innovation Office project No. **NKFIH_PD131848** and No. **VEKOP-2.3.2-16-2017-00013**.

Data availability Not applicable

Declarations

Ethics approval Not applicable.

Consent to participate The authors declare that they participated in this paper willingly.

Consent for publication The authors declare to consent to the publication of this paper.

Conflict of interest The authors declare no competing interests.

Open Access This article is licensed under a Creative Commons Attribution 4.0 International License, which permits use, sharing, adaptation, distribution and reproduction in any medium or format, as long as you give appropriate credit to the original author(s) and the source, provide a link to the Creative Commons licence, and indicate if changes were made. The images or other third party material in this article are included in the article's Creative Commons licence, unless indicated otherwise in a credit line to the material. If material is not included in the article's

Creative Commons licence and your intended use is not permitted by statutory regulation or exceeds the permitted use, you will need to obtain permission directly from the copyright holder. To view a copy of this licence, visit <http://creativecommons.org/licenses/by/4.0/>.

References

1. El-Galy IM, Saleh BI, Ahmed MH (2019) Functionally graded materials classifications and development trends from industrial point of view. *SN Appl Sci* 1:1. <https://doi.org/10.1007/s42452-019-1413-4>
2. Zhang C, Chen F, Huang Z, Jia M, Chen G, Ye Y, Lin Y, Liu W, Chen B, Shen Q, Zhang L, Lavernia EJ (2019) Additive manufacturing of functionally graded materials: a review. *Mater Sci Eng A* 764:138209. <https://doi.org/10.1016/j.msea.2019.138209>
3. Miyamoto Y, Kaysser WA, Rabin BH, et al (1999) *Functionally graded materials: design, processing and application*, Springer, Boston, MA, pp 1–317
4. Dudina DV, Bokhonov BB, Olevsky EA (2019) Fabrication of porous materials by spark plasma sintering: a review. *Materials (Basel)* 12:541
5. Askari E, Mehrali M, Metselaar IHSC, Kadri NA, Rahman MM (2012) Fabrication and mechanical properties of Al₂O₃/SiC/ZrO₂ functionally graded material by electrophoretic deposition. *J Mech Behav Biomed Mater* 12:144–150. <https://doi.org/10.1016/j.jmbbm.2012.02.029>
6. Ataollahi Oshkour A, Pramanik S, Mehrali M, Yau YH, Tarlochan F, Abu Osman NA (2015) Mechanical and physical behavior of newly developed functionally graded materials and composites of stainless steel 316L with calcium silicate and hydroxyapatite. *J Mech Behav Biomed Mater* 49:321–331. <https://doi.org/10.1016/j.jmbbm.2015.05.020>
7. Bódis E, Cora I, Balázsi C, Németh P, Károly Z, Klébert S, Fazekas P, Keszler AM, Szépvölgyi J (2017) Spark plasma sintering of graphene reinforced silicon carbide ceramics. *Ceram Int* 43:43–9011. <https://doi.org/10.1016/j.ceramint.2017.04.042>
8. Bódis E, Molnár K, Mucsi A, Károly Z, Móczó J, Klébert S, Keszler AM, Fazekas P, Szépvölgyi J (2017) Silicon nitride-based composites reinforced with zirconia nanofibres. *Ceram Int* 43:43–16818. <https://doi.org/10.1016/j.ceramint.2017.09.078>
9. Bódis E, Cora I, Németh P, Tapasztó O, Mohai M, Tóth S, Károly Z, Szépvölgyi J (2019) Toughening of silicon nitride ceramics by addition of multilayer graphene. *Ceram Int* 45:4810–4816. <https://doi.org/10.1016/j.ceramint.2018.11.176>
10. Balla A, Moczó J, Károly Z (2020) Co-ni-zn ferrites fabricated by spark plasma sintering. *Period Polytech Chem Eng* 64:64–270. <https://doi.org/10.3311/PPCh.14710>
11. Sweidan FB, Ryu HJ (2020) One-step functionally graded materials fabrication using ultra-large temperature gradients obtained through finite element analysis of field-assisted sintering technique. *Mater Des* 192:192. <https://doi.org/10.1016/j.matdes.2020.108714>
12. Belmonte M, Miranzo P, Osendi I (2015) Enhanced microstructural and mechanical gradients on silicon nitride ceramics. *Ceram Int* 41:41–2598. <https://doi.org/10.1016/j.ceramint.2014.10.006>
13. Munir ZA, Quach DV, Ohyanagi M (2011) Electric current activation of sintering: a review of the pulsed electric current sintering process. *J Am Ceram Soc* 94:1–19
14. Grasso S, Sakka Y, Maizza G (2009) Electric current activated/assisted sintering (ECAS): a review of patents 1906–2008. *Sci Technol Adv Mater* 10:10. <https://doi.org/10.1088/1468-6996/10/5/053001>
15. Anselmi-Tamburini U, Gennari S, Garay JE, Munir ZA (2005) Fundamental investigations on the spark plasma sintering/synthesis process: II. Modeling of current and temperature distributions. *Mater Sci Eng A* 394:139–148. <https://doi.org/10.1016/j.msea.2004.11.019>
16. Morin C, Le Gallet S, Ariane M, Bernard F (2016) Spark plasma sintering tool design for preparing alumina-based Functionally Graded Materials. *Ceram Int* 42:42–3063. <https://doi.org/10.1016/j.ceramint.2015.10.092>
17. Colasuonno PS (2017) Thesis method for creating functionally graded materials with spark plasma sintering and a continuous machine for future scalability [Master's thesis, Colorado State University, Fort Collins, Colorado]
18. Hulbert DM, Jiang D, Dudina DV, Mukherjee AK (2009) The synthesis and consolidation of hard materials by spark plasma sintering. *Int J Refract Met Hard Mater* 27:367–375. <https://doi.org/10.1016/j.jrmhm.2008.09.011>
19. Bódis E, Fábíán Á, Bán K et al (2017) Microstructure and sintering mechanism of SiC ceramics reinforced with nanosized ZrO₂. *Eur Chem Bull* 6:484. <https://doi.org/10.17628/ecb.2017.6.484-490>
20. Asimakopoulou A, Gkekak I, Kastrinaki G, Prigione A, Zaspalis VT, Petrakis S (2020) Biocompatibility of α -Al₂O₃ ceramic substrates with human neural precursor cells. *J Funct Biomater* 11. <https://doi.org/10.3390/JFB11030065>
21. Marti A (2000) Inert bioceramics (Al₂O₃, ZrO₂) for medical application. *Injury*. 31:D33–D36. [https://doi.org/10.1016/S0020-1383\(00\)80021-2](https://doi.org/10.1016/S0020-1383(00)80021-2)
22. Huang CY, Chen YL (2016) Design and impact resistant analysis of functionally graded Al₂O₃-ZrO₂ ceramic composite. *Mater Des* 91:294–305. <https://doi.org/10.1016/j.matdes.2015.11.091>
23. Xu C, Liu H, Yang H, Yang L (2016) A green biocompatible fabrication of highly porous functional ceramics with high strength and controllable pore structures. *J Mater Sci Technol* 32:729–732. <https://doi.org/10.1016/j.jmst.2016.07.002>
24. Bizot P, Sedel L (2001) Alumina bearings in hip replacement: theoretical and practical aspects. *Oper Tech Orthop* 11:263–269. [https://doi.org/10.1016/S1048-6666\(01\)80040-9](https://doi.org/10.1016/S1048-6666(01)80040-9)
25. Zhang Y, Sun MJ, Zhang D (2012) Designing functionally graded materials with superior load-bearing properties. *Acta Biomater* 8:8–1108. <https://doi.org/10.1016/j.actbio.2011.11.033>
26. Wu YQ, Zhang YF, Huang XX, Guo JK (2001) Preparation of platelike nano alpha alumina particles. *Ceram Int* 27:265–268. [https://doi.org/10.1016/S0272-8842\(00\)00074-2](https://doi.org/10.1016/S0272-8842(00)00074-2)
27. Lamouri S, Hamidouche M, Bouaouadja N, et al (2017) Control of the γ -alumina to α -alumina phase transformation for an optimized alumina densification. *Bol. la Soc. Esp. Ceram. y Vidr*. <https://doi.org/10.1016/j.bsecv.2016.10.001>
28. Zhang Y, Xie M, Roscow J, Bao Y, Zhou K, Zhang D, Bowen CR (2017) Enhanced pyroelectric and piezoelectric properties of PZT with aligned porosity for energy harvesting applications. *J Mater Chem A* 5:6569–6580. <https://doi.org/10.1039/c7ta00967d>
29. Zhang QS, Chen XB, Yang Q, Zhang WJ (2012) Development and characterization of a novel piezoelectric-driven stick-slip actuator with anisotropic-friction surfaces. *Int J Adv Manuf Technol* 61:1029–1034. <https://doi.org/10.1007/s00170-011-3771-y>

Publisher's note Springer Nature remains neutral with regard to jurisdictional claims in published maps and institutional affiliations.